



# Large-scale high-sensitivity optical diffraction tomography of zebrafish

JOS VAN ROOIJ\* AND JEROEN KALKMAN

*Department of Imaging Physics, Delft University of Technology, Lorentzweg 1, 2628 CJ Delft, The Netherlands*

*\*j.vanrooij@tudelft.nl*

**Abstract:** In this work we demonstrate large-scale high-sensitivity optical diffraction tomography (ODT) of zebrafish. We make this possible by three improvements. First, we obtain a large field of view while still maintaining a high resolution by using a high magnification over numerical aperture ratio digital holography set-up. With the inclusion of phase shifting we operate close to the optimum magnification over numerical aperture ratio. Second, we decrease the noise in the reconstructed images by implementing off-axis sample placement and numerical focus tracking in combination with the acquisition of a large number of projections. Although both techniques lead to an increase in sensitivity independently, we show that combining them is necessary in order to make optimal use of the potential gain offered by each respective method and obtain a refractive index (RI) sensitivity of  $8 \cdot 10^{-5}$ . Third, we optimize the optical clearing procedure to prevent scattering and refraction to occur. We demonstrate our technique by imaging a zebrafish larva over  $13 \text{ mm}^3$  field of view with 4 micrometer resolution. Finally, we demonstrate a clinical application of our technique by imaging an entire adult cryoinjured zebrafish heart.

© 2019 Optical Society of America under the terms of the [OSA Open Access Publishing Agreement](#)

## 1. Introduction

Three dimensional (3D) optical imaging is used in many areas of biology and medicine as is evidenced by the multitude of 3D imaging modalities that have been developed. Advantages of such techniques include the capability of virtual instead of physical sectioning and the possibility of quantitative 3D analysis in the original geometry. It is also possible to do 3D imaging of unlabeled samples making use of intrinsic contrast present in the sample [1,2]. One such contrast is the refractive index (RI) variation in the sample, which is often feature specific and provides information about the global structure in the sample (in contrast to molecular specific techniques). Optical diffraction tomography (ODT), sometimes also referred to as phase tomography, images the RI contrast by measuring the complex wavefront of the transmitted object wave. and is used to make quantitative images of the 3-D RI distribution of transparent samples. This is done by acquiring phase images of a sample from different angles, and combining these in a 3D reconstruction of the sample by using a back propagation algorithm. Besides imaging in a well defined geometry, phase tomography is also performed in microfluidic flow channel and is known as in-flow tomography [3,4].

Closely related to ODT is optical projection tomography (OPT), an established method to reconstruct 3-D fluorescence emission or attenuation in a sample. Although tomographic acquisition and reconstruction have common ground in both techniques, the two fields have been operating independently in some important respects. The most striking difference is the size scale at which ODT is applied compared to that in OPT. It is common in the field of OPT to image both small scale samples like cells [5] as well as large scale biological samples, like zebrafish (adult and embryo's) [6,7] or mouse brains [8], and OPT is considered especially useful in such millimeter scale samples [9]. ODT of biological tissue is mainly focused on small scale imaging and applied to samples in the tens of microns size range, such as cells [10,11] and (plant) fibers [12]. This is caused by the fact that on the one hand ODT relies on RI differences inside the

sample to be present for image formation. On the other hand ODT requires that RI differences are sufficiently small in order to prevent a change in direction of the rays passing through the object or severe aberrations of the wavefront to occur, both which inhibit accurate reconstruction of the object wavefield. In larger samples, even small changes in refraction can cause a major lateral displacement of the rays hitting the detector or cause large wavefront aberrations due to the larger optical path length through the object. Hence, even for small RI differences, deformation of the phase projection occurs, with a resulting poor imaging reconstruction as a result. Consequently, for large scale ODT of biological tissues, the RI variation must be small enough in order to minimize these effects, but the imaging method must be sensitive enough to still detect this RI variation in the wavefront and allow for sufficient contrast in the reconstructed image. Since this combination is challenging to obtain it is not surprising that attention in ODT research has mainly focused on small samples which are inherently transparent, like biological cells or (plant) fibers, that are in the range of 10 – 30  $\mu\text{m}$  in diameter, and thus do not cause significant beam deviation and wavefront aberrations when light propagates through the sample.

A recent exception is ODT applied to a large scale synthetic lens object with high phase sensitivity [13]. However, in this case the surrounding index matching liquid had to be very precisely matched to the RI of the lens. This kind of precise index matching only works for homogeneous samples. An alternative is to use optical clearing of the sample and image the sample in the clearing liquid. Optical clearing aims to homogenize the RI in a sample in order to increase imaging depth and image quality [14]. However, optical clearing causes RI differences to be (very) small, necessitating high sensitivity and therefore a low noise level in the reconstruction to obtain high quality images. Although the issues of deformation of the projections (due to ray displacement) and severe aberrations of the wavefront could then be solved, the challenge is then to accurately image the remaining RI contrast accurately.

In this paper, we demonstrate, to our knowledge for the first time, that high contrast and high resolution 3D refractive imaging of large scale biological samples can be done with phase tomography without extensive index matching procedures using the following steps:

- large scale high resolution imaging using a large image sensor and phase shifting digital holography to make full use of the spatial frequency bandwidth of the system.
- high sensitivity RI detection through off-axis sample placement combined, with numerical focus tracking during rotation, and acquisition of a large number of projections.
- minimization of scattering and refraction by using a passive optical clearing procedure common in OPT.

We demonstrate our large scale high resolution approach with measurements on a 3 day old zebrafish larva and an adult zebrafish heart for several reasons. First of all, zebrafish larvae have been studied in detail in 3D using OPT, facilitating comparison and validation of our results. Second, zebrafish larvae are clinically relevant since they have been widely used as models to gain insight in human disease [15]. ODT adds an additional type of contrast (RI) to large scale organic tissue imaging not traditionally accessible in OPT, which allows for imaging of structures such as eyes, brains and yolk sack using intrinsically present RI contrast. Finally, we demonstrate a clinically relevant application where we image regenerating zebrafish heart tissue after damage based on RI contrast and estimate the relative volume of the injured tissue. This can eliminate the need for the current labour intensive procedure of sectioning and staining of the heart [16].

## 2. Materials and methods

### 2.1. Acquisition of phase projections

In ODT, the scattered field is recorded from multiple angles using digital holography. The digital holography setup is shown in Fig. 1 and consists of a Mach-Zehnder interferometer operated in

transmission. The light source is a HeNe laser with a wavelength of 633 nm and an output power of 3 mW. Two lenses (Thorlabs, LD2568 and LA1979) are used to expand and collimate the illuminating laser beam respectively to a full width at half maximum (FWHM) of approximately 15 mm.

In the object arm a 4X Super Apochromatic objective lens ( $NA = 0.2$ ) is used in combination with a 200 mm focal length tube lens (both Thorlabs) to image the sample on the CMOS camera, (Basler beA4000-62kc) with 4096 x 3072 pixels and a pixel pitch of 5.5 micrometer. A rotation mount (Thorlabs CR1) rotates the sample stepwise over 360 degrees. The sample is displaced from the center of rotation by approximately 1 mm in order to suppress noise in the reconstruction of the sample caused by fixed pattern coherent speckle [17]. In the reference arm, a 4X Olympus microscope objective partly compensates for the object wave curvature to avoid the presence of too high spatial frequencies on the camera. The mirror in the reference arm is mounted onto a piezoelectric transducer controlled by a computer for phase-shifting the digital hologram. We capture four holograms with (reference arm) phase shift increments of  $\pi/2$  between each subsequent hologram. From a linear combination of these holograms a complex hologram is formed where the zeroth and out of focus conjugate orders are removed [18]. In this way we maximize the lateral resolution in the reconstructed image. This is specifically important for large scale ODT where magnification is low but an as high as possible  $NA$  is desired, as we will show in the following section. After acquiring the complex hologram, autofocus correction in the reconstruction of the digital hologram is applied in order to obtain the wavefield in the object region. For off-axis sample placement the object position as a function of the projection angle is a sinusoidal function. To find the object position we calculate a focus metric (grayscale variance) as a function of the reconstruction distance for ten samples of a full rotation acquisition (i.e.  $0^\circ$ ,  $36^\circ$ ,  $72^\circ$  and so on). For transparent objects, the grayscale variance has a minimum value when the reconstruction distance is located at the object [17], in contrast to imaging reflective samples where the grayscale variance has a maximum [19]. A sinus function is fitted to the data to retrieve the object distance as a function of projection angle. The hologram is then (for each angle separately) reconstructed with the object in focus by back propagating the field from the detector plane to the object plane using the angular spectrum method for diffraction calculation, which is exact (apart from the scalar approximation to the wave equation) and thus suitable for propagating over small distances. The phase is then calculated by taking the argument of the reconstructed wavefield. Since the phase change in a projection mostly exceeds  $2\pi$ , the phase is unwrapped using a least squares phase unwrapping algorithm [20].

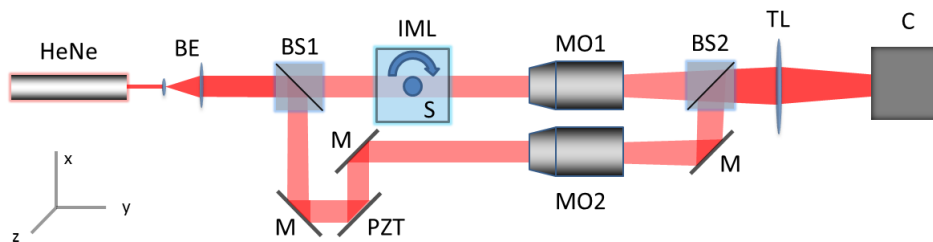


Fig. 1. Experimental setup for acquiring the digital holograms. HeNe: Helium Neon laser, BE: Beam expander, BS: Beam splitter, IML: Index matching liquid, S: Sample rotated around the z-axis, MO: Microscope objective, M: Mirror, TL: Tube lens, PZT: Mirror mounted on piezo stage, C: Camera.

## 2.2. Optimizing ODT resolution and field of view

In conventional microscopy, in order to meet the Nyquist sampling criterion, it must hold that  $\eta \geq 2\xi$ , where  $\eta$  is the projected feature size and  $\xi$  is the pixel pitch of the camera. In off-axis digital holography, diffraction orders appear that must be spatially separated by introducing an angle between the object beam and the reference beam. In order to separate the twin images, neglecting the frequency content in the zeroth order for simplicity, only half of the spatial frequency bandwidth offered by the camera is available, i.e.  $\eta \geq 4\xi$ . The smallest resolvable feature that can be imaged with a microscope objective is  $\Delta x = 0.61\lambda/NA$  according to the Rayleigh criterion. Hence, for a point object projected onto the camera sensor by an objective with magnification  $M$ , the condition

$$\frac{0.61\lambda}{NA} M \geq 4\xi \quad (1)$$

must be met in order to satisfy the Nyquist sampling criterion and separate the twin images. For the camera pixel size  $\xi = 5.5 \cdot 10^{-6}$  m and wavelength  $\lambda = 633 \cdot 10^{-9}$  m the ratio between magnification and numerical aperture to make full use of the available resolution is

$$\frac{M}{NA} \gtrsim 57. \quad (2)$$

Since typical  $NA$  values are between 0 and 1 only microscope objectives with high magnification use the spatial frequency bandwidth of the camera without loss in resolution. In large scale ODT, it is desirable to use a low magnification to image a relatively large object onto the camera while having an as high as possible  $NA$  to maximize the resolution. In a standard off-axis configuration this results in a significant loss in resolution. In the setup in this paper we have  $M/NA = 20$ . Since, by applying phase shifting there are no twin images, Eq. (2) reduces to  $M/NA \geq 28$  and hence, our ODT imaging set-up configuration is close to the optimum configuration for large scale high resolution ODT.

## 2.3. Noise suppression in large scale ODT

In large scale ODT, RI contrast should be small enough not to cause severe ray displacements and aberrations as a result of light propagation through the sample. Optical clearing of the samples reduces the RI contrast significantly to make the samples suitable for imaging. However, at the same time the contribution of the noise relative to the RI contrast will increase as a result, decreasing the effective sensitivity of the ODT reconstruction. Noise suppression therefore plays an important role, especially in large scale ODT, to obtain high quality images. The noise in the phase projections originates from intensity noise in the digital hologram (assuming perfect phase unwrapping). The noise in the digital hologram translates into the phase noise in a highly non-linear way and an in depth discussion is beyond the scope of this paper. Two sources of intensity noise that contribute to the phase noise can be identified, namely fixed speckle noise in the digital hologram that is constant for each projection [17] and variable noise that changes from projection to projection (e.g. due to read-out or shot noise), which we call incoherent noise. Two methods can be used to reduce the noise levels. The first noise suppression method was proposed by Kostencka et al. [17], where they argue that placing the sample at the center of rotation (as is generally done to keep the sample in focus) leads to more noise in the reconstruction as the speckle noise is spread over a circle in the reconstructed image with radius equal to the off-axis distance. By displacing the sample with respect to the center of rotation the noise is spread over a larger circle in the reconstructed image, and hence is strongly decreased. Kostencka et al. reported a reduction in the reconstruction error by a factor between 2 and 7, depending on the sample size.

Besides the fixed speckle noise, there is noise in the phase projections resulting from incoherent (shot and read) noise fluctuations in the recorded digital holograms. Since this type of noise varies from hologram to hologram it thus leads to variable phase noise in the projections, and can be mitigated through averaging. We suppress this noise with an increase in the number of projections, since backprojection is akin to averaging of projections for each pixel. This is analogous to what is common in signal processing, where signal averaging increases the strength of the signal relative to the noise. More specifically, averaging  $N$  realizations of the same, uncorrelated noise reduces the standard deviation by a factor  $\sqrt{N}$ .

We expect that in the region close to the center of rotation, the first kind of (angle independent) speckle noise dominates the noise level, and that an increase in the number of projections is less effective in suppression of the noise than displacing the sample of axis. Further away from the center of rotation, we expect the contribution due to the speckle noise to be small, and thus further displacing the sample away from the center of rotation will not give significant improvements. Instead, we expect that off-axis the incoherent noise dominates the noise level, and that increasing the number of projections dominates further improvement in terms of noise suppression according to the  $\sqrt{N}$  law. Thus, we expect that noise suppression with an increasing number of projections is effective mainly outside of the center of rotation.

To quantify the noise level, we take the standard deviation of the RI difference values in a collection of voxels of a constant RI part of optically cleared agarose. This is in line with the approach of Kim et al. [13], where they associate the standard deviation of a constant background reconstruction with the sensitivity of the ODT reconstruction. In Fig. 2(b), the standard deviation at the axis of rotation (purple circle in Fig. 2(a)) and outward towards the edge of the sample (red circle in Fig. 2(a)) is plotted as a function of the number of projections. It is clear that increasing the number of projections as well as moving the sample radially outward significantly reduces the noise level, increasing the sensitivity up to approximately a factor 4 for 1440 projections compared to on-axis placement of the sample with 360 projections. Furthermore, in Fig. 2(b), a curve  $\sigma = a \cdot N_p^{-0.5}$  is fitted to the off axis noise level, where  $N_p$  represents the number of projections and  $a$  is a constant. The accuracy of the fit confirms the expectation that away from the center of rotation, the incoherent noise type dominates and reduces with the square root of the number of projections. In the center of rotation the decrease in noise as a function of the number of projections is limited due to the presence of the fixed speckle noise, which is indicated by a horizontal line in Fig. 2(b). In Fig. 2(c), the reciprocal of the variance curve (also called the precision or variability) increases linearly with the number of projections in the off-axis case as expected, but stays nearly constant for the on-axis case. Figure 2(d) shows the noise standard deviation through a cross section of the reconstructed object. It shows that the noise level at the center of rotation is similar for 144 and 1440 projections, whereas it differs significantly away from the center of rotation. The noise level can be seen to be approximately constant around half a millimetre away from the center, and further sample displacement will not yield significant noise reduction. Thus, for on-axis placement an increase of the number of projections will not yield significant noise reduction, and away from the center of rotation the variable phase noise (e.g. due to read-out and shot noise) dominates and can be effectively reduced by increasing the number of projections. The fact that the sample must be off-axis (to guarantee low noise) does however reduce the field of view, in our case by almost a factor 8, to approximately  $13 \text{ mm}^3$ . This was estimated by calculating the area of the largest possible circle in a region starting approximately 0.5 mm away from the center of rotation, until the edge of the horizontal field of view, and multiplying this by the vertical field of view to obtain the volume.

#### 2.4. Tomographic image reconstruction

For reconstruction of the digital hologram, the angular spectrum method is used. The phase distribution at the in-focus position is then unwrapped using a least squares phase unwrapping

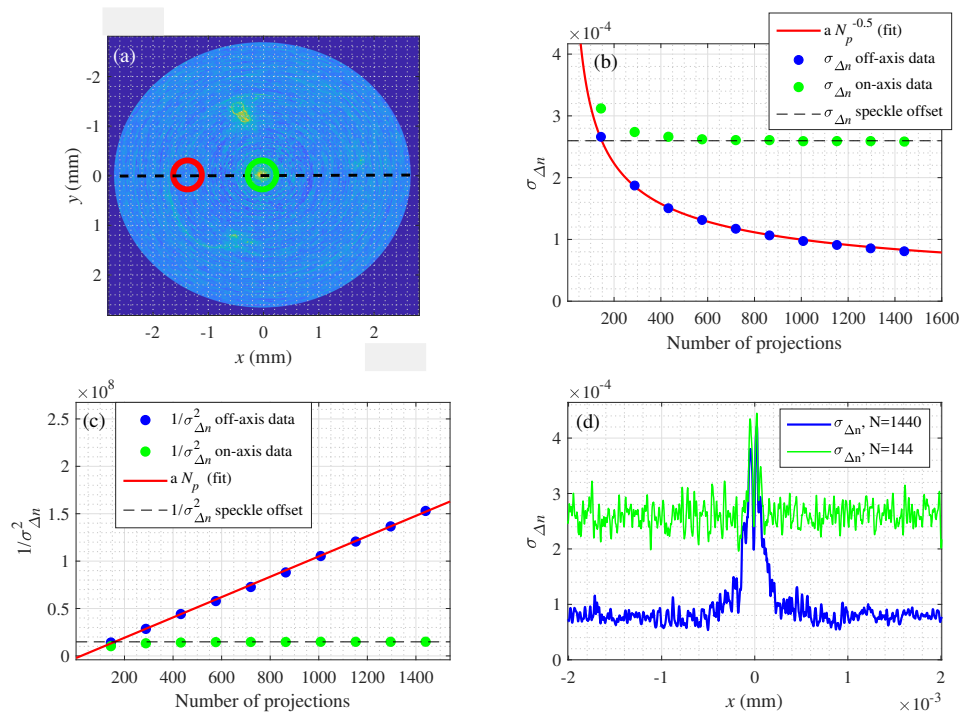


Fig. 2. (a) Reconstruction of a horizontal cross-section of the agar sample indicating the a point close to the center of rotation (green circle) and one 1 mm radially outward (red circle). (b) Noise levels at the center of rotation and 1.5 mm radially outward as a function of the number of projections ( $N_p$ ), with  $y = a N_p^{-0.5}$  fitted to the off-axis data and the on-axis noise limit indicated by a constant. (c) Plot of the precision, defined as the inverse of the variance, of the same data and model as in (b), with  $y = a N_p$  fitted to the off-axis data and the on-axis noise limit indicated by a constant. (d) Noise levels as a function of distance to the center for 1440 and 144 projections respectively (cross-section horizontally through the middle in (a)).

technique [20]. Assuming that RI variation in the sample is sufficiently small so that refraction does not occur, a phase projection can be regarded as a scaled integral over the RI variation with respect to the background medium along the illumination direction. The 3D relative RI ( $\Delta n$ ) structure of the object is reconstructed using the filtered back projection (FBP) algorithm, in which case reconstruction can be performed for each transverse slice separately. In this study, we perform tomographic reconstruction with 1440 projections over 360 degrees (steps of 0.25 degrees) with four phase steps per projection. The net acquisition time is approximately 7 minutes. The total acquired data in this case is around 20 GB, which fits in the internal memory of a 32 GB RAM desktop PC. The complete algorithm flowchart is depicted in Figure 3.

### 2.5. Characterization of resolution

We characterized the spatial resolution of the setup using a FEP-tube with an inner diameter of 0.9 mm embedded in a 9 % mass-percentage glucose/water solution. The spatial resolution is estimated based on the edge response from the inner boundary between the FEP-tube and the liquid (at 0.45 mm from the center of rotation) along the  $x$ -axis (where  $z$  is the vertical axis, and the  $y$ -axis the optical axis). For a reconstruction based on 1440 projections, the resolution is

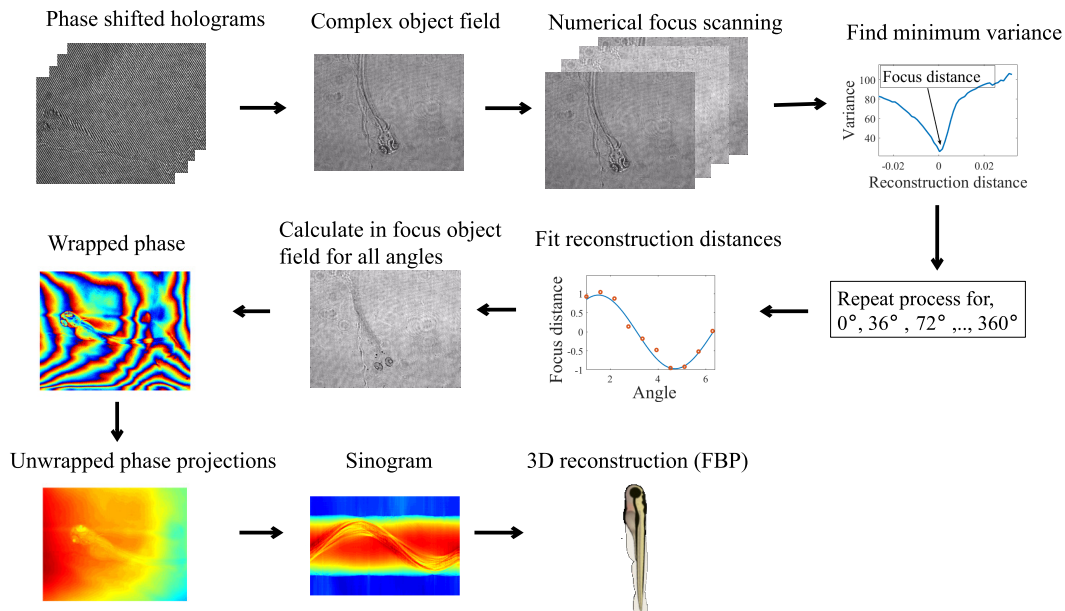


Fig. 3. Flowchart that shows schematically the steps from acquisition of the phase shifted holograms to the final 3D reconstruction.

measured to be 4 micrometer.

## 2.6. 3D data visualisation

In order to discern different features in the zebrafish samples, we estimated the mean relative RI of different parts of the zebrafish larva by calculating the  $\Delta n$  distribution of a sub volume inside that feature. We used the Drishti software package [21] with a non-linear transfer function of  $\Delta n$  based on the  $\Delta n$  distributions of different zebrafish features for the visualisation.

## 2.7. Sample preparation: 3 day old zebrafish larva

The sample is a 3 day old zebrafish embryo (wild type). The eggs are grown on a petridish and subsequently placed in PTU (1-phenyl 2-thiourea) to prevent pigment formation. At 72 hours, the eggs are dechorionated and fixated in 4 % paraformaldehyde. Then, the eggs are washed with Phosphate buffered saline tween-20 three times, after which it is replaced with 100% MeOH in two cycles for dehydration. The embryos are placed in small cylinders (4 mm diameter) and mixed with agarose (2% mass-percentage). After the agarose is dry, the agarose containing the embryo's is removed from the cylinders and as a whole placed in BABB, a mixture of benzyl alcohol (Sigma B-1042) and benzyl benzoate (Sigma B-6630) in a 1:2 ratio, to make the sample completely transparent. During this process, the RI of the sample becomes almost that of the BABB clearing solution. The optimal clearing time ensures that the sample is transparent enough for optical phase tomography, while at the same time maximizing remaining RI contrast in order to keep a good signal (RI contrast in the reconstruction) to noise (background) ratio in the final reconstruction. We used a clearing time of 3 hours that we estimate is the optimal time that fulfills the above mentioned criterion.

### 2.8. Sample preparation: damaged zebrafish heart

The heart is extracted from a one-year-old zebrafish. Seven days before extraction, the heart is damaged through cryoinjury. This is done by anesthetizing the fish in tricaine, after which the chest is opened and the heart is damaged with a copper needle cooled in liquid nitrogen [22]. 7 days after damaging the hearts, the fish is euthanized in icewater. The heart is then isolated in phosphate buffered saline), KCl (Potassium chloride) and heparin. After fixation, the heart is dehydrated, mounted in an agarose (2% mass-percentage) cylinder and placed in BABB solution like the zebrafish samples in the previous section.

## 3. Results

### 3.1. Large-scale zebrafish ODT

Virtual cross-sections of our large-scale zebrafish ODT reconstructions of the sample are shown in Figs. 4(a)–4(c) where  $\Delta n$  is quantitatively visualized on a linear gray scale. The  $\Delta n$  distribution of the reconstructed background (optically cleared agarose) is depicted in Fig. 4(d) and found to have a standard deviation of  $\sigma = 8 \cdot 10^{-5}$ . Visualization of different structures is done based on the RI difference distribution plotted in the histogram in Fig. 5(f) on a logarithmic scale, and is shown in Fig. 5. The RI distribution of an organ was estimated by scaling the distribution of a sub-volume of that organ to the maximum in the histogram. The brain tissue, for example, is distributed around  $\Delta n = 2.2 \cdot 10^{-3}$  (visualized in blue in Fig. 5), the interstitial tissue is centered around  $\Delta n = 7.5 \cdot 10^{-4}$  (visualized in green), and the yolk sac appears in the distribution centered around  $\Delta n = 2.0 \cdot 10^{-4}$  (visualized in red). Due the small volume of the eyes and the relatively high RI, it is not visible in Fig. 5(f), but has a RI of around  $\Delta n = 1 \cdot 10^{-2}$  and is visualized in red in Figs. 5(d) and 5(f). We compared our results with image reconstructions of a 3 day old zebrafish larva from The Atlas of Zebrafish Development that were obtained through OPT and found comparable anatomic structures, as is evident from comparing (for example) Fig. 5(b) and Fig. 5(e) with figures 6.68 and 6.10-6.12 from the atlas respectively [23].

### 3.2. Large-scale zebrafish heart ODT

Virtual cross-sections of the zebrafish heart are shown in Fig. 6. Different parts of the heart can be discerned, such as the injured area (IA), the ventricle (V), the bulbus (B) and the atrium (A). The damaged part of the heart is correctly segmented using a region growing algorithm based on RI values of the image [24], and is indicated in the bounded area (red) in Fig. 6 (a). The  $\Delta n$  range of the entire heart is found to be comparable to that of the zebrafish larva. The RI distribution of the regenerating tissue was compared to the cleared agarose background and found to have the same mean, but larger standard deviation, since less structure appears in the regenerating tissue. This is as expected, as the zebrafish was euthanized 7 days after cryoinjury, whereas full recovery after cryoinjury takes approximately 2 months. We estimate the relative volume of the injured part to be approximately  $14 (\pm 0.5)\%$  of the total heart volume through manual slice by slice segmentation of the 3D reconstruction. This estimate is in line with histological studies of zebrafish regeneration, e.g. Chablais et al. who found an average of relative scar volume between 13.5% and 18.5% in 6 samples aged between 6-18 months and with a similar cryoinjury procedure [25].

## 4. Discussion and conclusions

In this paper, we showed for the first time, to the best of our knowledge, the viability of high resolution and high sensitivity 3D RI imaging of millimeter sized biological samples using ODT. Previously, this has only been achieved using OPT, or with ODT on non-organic homogeneous samples [13], using careful index matching to obtain a low RI contrast (and thus low scattering) and high sensitivity. Optical clearing proved to be an easy to implement solution to make samples

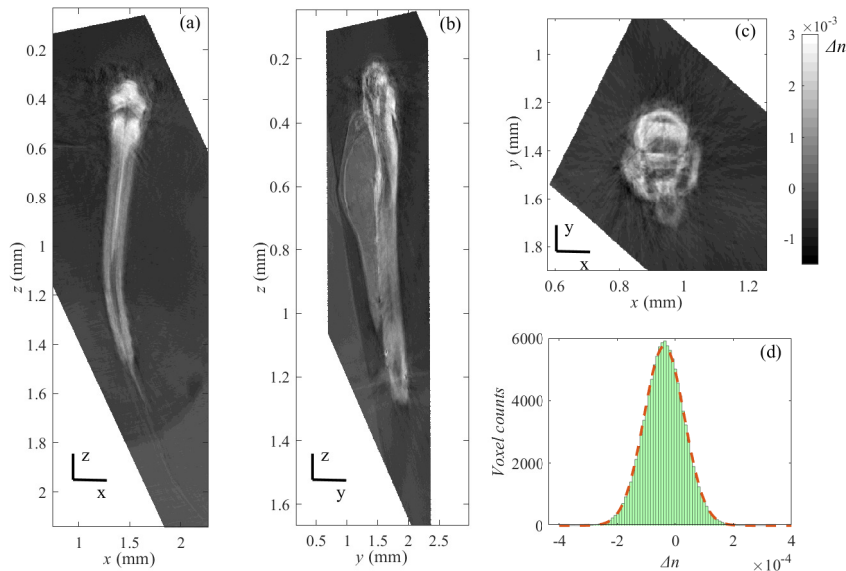


Fig. 4. (a-c) Coronal, sagittal, and axial cross-sections of ODT reconstructed refractive index contrast of an optically cleared 3 day old zebrafish larva. (d)  $\Delta n$  distribution of agarose background in which the zebrafish sample is placed. From this the sensitivity in the reconstruction was calculated as the standard deviation of the distribution and yields  $\sigma = 8 \cdot 10^{-5}$ .

sufficiently transparent for ODT, while still retaining relevant RI contrast to segment different organs and features in the zebrafish larva and zebrafish heart. Optimizing the clearing time to approximately 3 hours and the system sensitivity were found to be important for obtaining high quality images. We showed that high RI sensitivity can be achieved by using noise suppression of two independent noise sources. We achieved this by combining off-axis placement of the sample and auto-focus correction together with the acquisition of a large number of projections. Although both techniques lead to an increase in sensitivity independently, we showed that combining them is necessary in order to make optimal use of the potential gain offered by each respective method. In this way, high RI sensitivity can be achieved that is necessary for phase tomography of optically cleared large scale organic tissue. We demonstrate the identification of tissue structures with features in the order of  $\Delta n = 6 \cdot 10^{-4}$  with respect to the background and, based on this RI contrast, are able to segment it from the background. Finally, we demonstrated a possible clinical application where regenerating zebrafish heart tissue could be detected and segmented based on RI contrast, and quantified the relative volume of the injured area (after cryoinjury) of a zebrafish heart. Although we did this manually, this can make it possible to study heart regeneration quantitatively in an automated fashion without labour intensive staining, sectioning, and manual estimating of the volumes. To underline this potential, we demonstrated automated segmentation of the injured area using a region growing algorithm on a single slice.

Large scale high sensitivity ODT imaging comes at the cost of the acquisition and processing of large data sets which is challenging to handle even with today's powerful desktop computers. Using phase shifting digital holography in large scale ODT, unlike in cases with high magnification, proved necessary for a high resolution with a large field of view but further increases the amount of data. The phase images are reconstructed using filtered back projection, which assumes that rays traverse the object in straight paths and no diffraction takes place. Although this is not a strictly valid assumption, this was done in view of the large dataset; phase projections

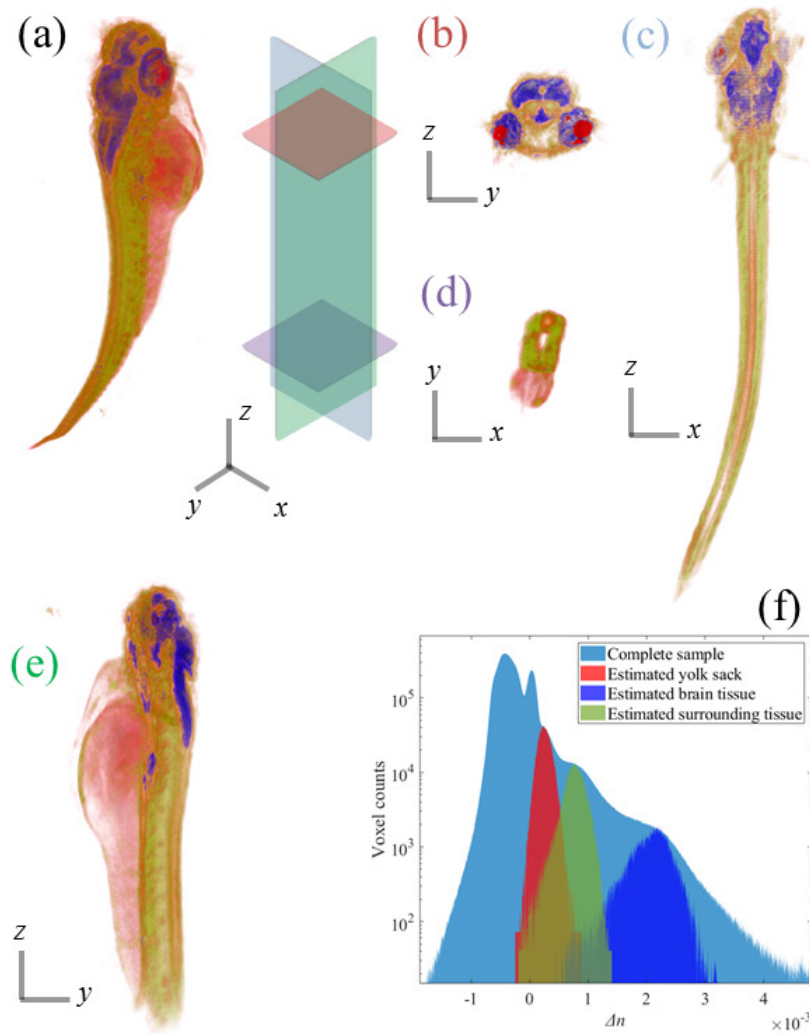


Fig. 5. A 3D visualization of a complete zebrafish larva (3 days old) based on RI differences is shown in (a) and for different cross-sections in (b-e). In (f), a logarithmic plot is shown of the RI distribution of the complete sample (zebrafish larva and agarose). Indicated are the estimated  $\Delta n$  distributions of different types of tissue in the zebrafish larvae. The first two peaks in blue from the left are from the agarose and index matching liquid (BABB) contributions respectively.

obtained with 12 Megapixels lead to a dataset of over 100 GB for 1440 projections. In current implementations of ODT using the Rytov approximation the total data should fit in memory at one time in order to do the reconstruction, which is far more than typically available even on powerful desktop computers. FBP allows slice by slice reconstruction, circumventing the memory issue, but at the same time gives a non-isotropic resolution (with resolution deteriorating away from the focus position). We expect this effect to be limited for zebrafish larva due to the relatively small dimensions in the axial plane and digital refocusing that was applied. However, for large scale ODT on samples with isotropic dimensions and with high (isotropic) resolution we therefore think it is necessary that ODT implementations are developed that allow for step by

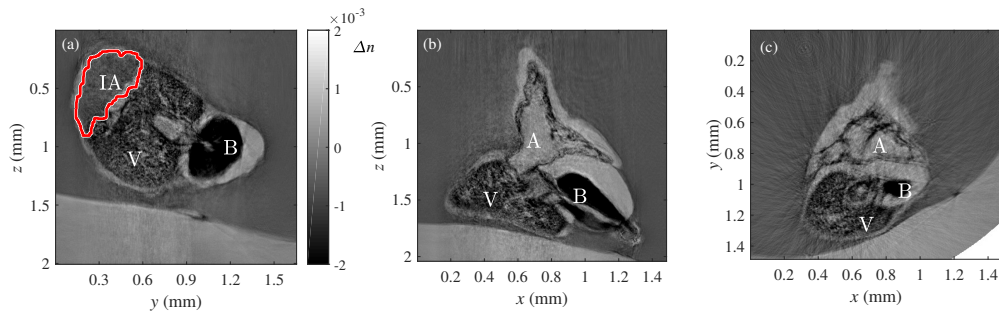


Fig. 6. Virtual cross-sections in the  $y$ - $z$  plane (a),  $x$ - $y$  plane (b) and the  $x$ - $z$  plane (c) showing the  $\Delta n$  distribution of a 1 year old zebrafish heart, damaged through cryoinjury. The regenerating tissue can be seen in the bounded region (red) in image (a) obtained through region growing segmentation. Features can be seen such as the injured area (IA), the ventricle (V), the bulbus (B) and the atrium (A).

step reconstruction of the 3D reconstruction, thereby reducing the memory needed at one time, instead of solving the inverse diffraction problem on the entire dataset.

The large data sets in large scale ODT with high sensitivity and high resolution also come at the cost of long computation times. The phase unwrapping takes approximately 1.5 hours for 1440 projections, whereas the filtered back projection takes approximately 10 hours to complete for all the slices. The time it takes to do a complete 3D reconstruction of a zebrafish is thus approximately 12 hours. Apart from using the four available cores in parallel to do the calculations, we did not optimize the reconstruction algorithm, but expect that significant improvements in computational speed are still possible, for example through using CUDA programming of the FBP reconstruction [26].

Finally, the zebrafish is relatively long compared to its width. Hence, in order to fit the complete zebrafish larva on the sensor, the magnification should be in the order of 4X for a 12 Megapixel camera. In the vertical direction the image plane (and thus resolution) was therefore used efficiently, but not in the lateral direction. Since the region of interest is usually the brain, the field of view can be restricted to this part of the sample and imaged at a higher magnification (10X) to obtain a higher resolution. The zebrafish heart was more isotropic in size, and can be studied at a higher magnification (10X) without losing part of the sample. It is important however to still keep sufficient unused space laterally in the image plane in order to apply off-axis placement of the sample. We envision that the method presented by us opens the door to application of ODT as a label-free diagnostic tool for studying a wider variety of clinically relevant and larger organic samples than what has been previously done, for example for studying cleared human tissue.

## Funding

Stichting voor de Technische Wetenschappen (STW); Netherlands Organisation for Scientific Research (NWO); Ministerie van Economische Zaken (EZ).

## Acknowledgments

We would like to thank Sonja Chocron, Hessel Honkoop, and Jeroen Bakkers (Hubrecht Institute) for providing zebrafish larvae and hearts. Furthermore, we thank Jelle van der Horst for help with visualization in Drishti.

## Disclosures

The authors declare that there are no conflicts of interest related to this article.

## References

1. J. Bailleul, B. Simon, M. Debailleul, L. Foucault, N. Verrier, and O. Haeberlé, "Tomographic diffractive microscopy: Towards high-resolution 3D real-time data acquisition, image reconstruction and display of unlabeled samples," *Opt. Commun.* **422**, 28–37 (2018).
2. K. Kim, W. S. Park, S. Na, S. Kim, T. Kim, W. D. Heo, and Y. Park, "Correlative three-dimensional fluorescence and refractive index tomography: bridging the gap between molecular specificity and quantitative bioimaging," *Biomed. Opt. Express* **8**, 5688–5697 (2017).
3. M. M. Villone, P. Memmolo, F. Merola, M. Mugnano, L. Miccio, P. L. Maffettone, and P. Ferraro, "Full-angle tomographic phase microscopy of flowing quasi-spherical cells," *Lab Chip* **18**, 126–131 (2018).
4. N. C. Pégard, M. L. Toth, M. Driscoll, and J. W. Fleischer, "Flow-scanning optical tomography," *Lab Chip* **14**, 4447–4450 (2014).
5. B. Belay, J. T. Koivisto, K. Vuornos, T. Montonen, O. Koskela, M. Lehti-Polojärvi, S. Miettinen, M. Kellomäki, E. Figueiras, and J. Hyttinen, "Optical projection tomography imaging of single cells in 3D gellan gum hydrogel," in *EMBECC & NBC 2017*, H. Eskola, O. Väisänen, J. Viik, and J. Hyttinen, eds. (Springer Singapore, 2018), pp. 996–999.
6. A. Bassi, L. Fieramonti, C. D'Andrea, M. C. Mione, and G. Valentini, "In vivo label-free three-dimensional imaging of zebrafish vasculature with optical projection tomography," *J. Biomed. Opt.* **16**(10), 100502 (2011).
7. T. Correia, N. Lockwood, S. Kumar, J. Yin, M.-C. Ramel, N. Andrews, M. Katan, L. Bugeon, M. J. Dallman, J. McGinty, P. Frankel, P. M. W. French, and S. Arridge, "Accelerated optical projection tomography applied to in vivo imaging of zebrafish," *PLOS ONE* **10**, 1–17 (2015).
8. T. Alantaló, A. Asayesh, H. Morrison, C. Lorén, D. Holmberg, J. Sharpe, and U. Ahlgren, "Tomographic molecular imaging and 3D quantification within adult mouse organs," *Nat. Methods* **4**, 31–3 (2006).
9. J. Sharpe, *Optical Projection Tomography* (Springer Berlin Heidelberg, Berlin, Heidelberg, 2009), pp. 199–224.
10. Y. Sung, W. Choi, C. Fang-Yen, K. Badizadegan, R. R. Dasari, and M. S. Feld, "Optical diffraction tomography for high resolution live cell imaging," *Opt. Express* **17**, 266–277 (2009).
11. M. Kujawińska, W. Krauze, A. Kus, J. Kostencka, T. Kozacki, B. Kemper, and M. Dudek, "Problems and solutions in 3D analysis of phase biological objects by optical diffraction tomography," *Int. J. Optomechatronics* **8**, 357–372 (2014).
12. M. Malek, H. Khelifa, P. Picart, D. Mounier, and C. Poilâne, "Microtomography imaging of an isolated plant fiber: a digital holographic approach," *Appl. Opt.* **55**, 111–121 (2016).
13. K. Kim, J. Yoon, and Y. Park, "Large-scale optical diffraction tomography for inspection of optical plastic lenses," *Opt. Lett.* **41**, 934–937 (2016).
14. D. S. Richardson and J. W. Lichtman, "Clarifying tissue clearing," *Cell* **162**, 246–257 (2015).
15. Y. M. Bradford, S. Toro, S. Ramachandran, L. Ruzicka, D. G. Howe, A. Eagle, P. Kalita, R. Martin, S. A. T. Moxon, K. Schaper, and M. Westerfield, "Zebrafish models of human disease: Gaining insight into human disease at ZFIN," *ILAR J.* **58**, 4–16 (2017).
16. S.-L. Lai, R. Marín-Juez, P. L. Moura, C. Kuenne, J. K. H. Lai, A. T. Tsedeke, S. Guenther, M. Looso, and D. Y. Stainier, "Reciprocal analyses in zebrafish and medaka reveal that harnessing the immune response promotes cardiac regeneration," *eLife* **6**, e25605 (2017).
17. J. Kostencka, T. Kozacki, M. Dudek, and M. Kujawińska, "Noise suppressed optical diffraction tomography with autofocus correction," *Opt. Express* **22**, 5731–5745 (2014).
18. I. Yamaguchi and T. Zhang, "Phase-shifting digital holography," *Opt. Lett.* **22**, 1268–1270 (1997).
19. J. van Rooij and J. Kalkman, "Sub-millimeter depth-resolved digital holography," *Appl. Opt.* **56**, 7286–7293 (2017).
20. D. C. Ghiglia and L. A. Romero, "Robust two-dimensional weighted and unweighted phase unwrapping that uses fast transforms and iterative methods," *J. Opt. Soc. Am. A* **11**, 107–117 (1994).
21. A. Limaye, "Drishti: a volume exploration and presentation tool," *Proc. SPIE 8506, Dev. X-Ray Tomogr. VIII*, 85060X (2012).
22. J. M. González-Rosa and N. Mercader, "Cryoinjury as a myocardial infarction model for the study of cardiac regeneration in the zebrafish," *Nat. Protoc.* **7**, 782–788 (2012).
23. R. Bryson-Richardson, S. Berger, and P. Currie, "Chapter 6 - 72 hours," in *Atlas of Zebrafish Development*, R. Bryson-Richardson, S. Berger, and P. Currie, eds. (Academic Press, San Diego, 2012), pp. 55–76.
24. D.-J. Kroon, *Region growing algorithm (m-file)* (MathWorks, Accessed 2 Dec. 2019).
25. F. Chablais, J. Veit, G. Rainer, and A. Jaźwińska, "The zebrafish heart regenerates after cryoinjury-induced myocardial infarction," *BMC Dev. Biol.* **11**, 21 (2011).
26. W. Krauze, A. Kus, D. Sladowski, E. Skrzypek, and M. Kujawińska, "Reconstruction method for extended depth-of-field optical diffraction tomography," *Methods* **136**, 40–49 (2018).